Editors' Suggestion | Featured in Physics

Observation of Lump Solitons

Ludovica Dieli,[1,2,*] Davide Pierangeli,[1,3,†] Fabio Baronio,[4] Stefano Trillo,[5] and Claudio Conti[1,2]
[1]Department of Physics, Sapienza University, 00185 Rome, Italy
[2]Enrico Fermi Research Center (CREF), 00184 Rome, Italy
[3]Institute for Complex Systems, National Research Council, 00185 Rome, Italy
[4]Department of Information Engineering, University of Brescia, 25123 Brescia, Italy
[5]Department of Engineering, University of Ferrara, 44122 Ferrara, Italy

(Received 27 June 2025; revised 26 November 2025; accepted 12 December 2025; published 6 February 2026)

Solitons are the cornerstone of nonlinear physics. The integrability of nonlinear equations is the basis of this universal concept. However, most multidimensional systems lack integrability, a fundamental limitation that challenges the existence of solitons in high dimensions. A remarkable exception would be the lump soliton, a two-dimensional solution of the Kadomtsev-Petviashvili (KP) equation with the unique property of propagating unperturbed in three-dimensional space. Due to the difficulty of implementing the KP dynamics in any physical system, lump solitons have never been observed. Here, we report the first experimental observation of the lump soliton. The lump is realized in nonlinear optics, in a photorefractive crystal under the action of paraxial diffraction and defocusing nonlinearity, ruled by the $(2+1)$D nonlinear Schrödinger (NLS) equation. We tailor the input field shape and the nonlinearity to realize the hydrodynamic KP integrable regime of the NLS equation. The lump emerges as a self-localized wave that propagates unaltered with a transverse velocity. We confirm its integrable nature by reporting, for the first time, the elastic collision of lumps in two dimensions. As the first experimental evidence of integrable solitons in high dimensions, our observation paves the way for a new era in the study of nonlinear systems.

DOI: 10.1103/ggbs-y21w

Introduction—Key advances in physics are propelled by our understanding of the underlying nonlinear partial differential equations (PDEs). The special property of integrability, valid for the restricted class of PDEs having an infinite number of conserved quantities, plays a pivotal role allowing fundamental predictions, such as the existence of solitons, and a closed-form description of complex nonlinear dynamics. Whether integrability is considered a surprising mathematical property or a well-expected manifestation of universal properties of nature such as symmetries or space-time homogeneity, there is no doubt that it has deeply driven experimental physics of $(1+1)$D systems for decades. Indeed, solutions via inverse scattering transform [1,2] of widespread models such as the Korteweg–de Vries and nonlinear Schrödinger (NLS) equations have provided the interpretation of observations in many different physical settings, ranging from BECs to plasma, water waves, and laser light in optical fibers and nonlinear crystals. Fundamental phenomena recently observed owing to integrability-based predictions encompass soliton collisions [3], the Peregrine soliton [4,5] and its universal role in the overfocusing catastrophe [6], the onset of super-regular breather from modulation instability [7], the statistics of rogue waves [8–10], multisoliton fission [11,12], the Fermi-Pasta-Ulam-Tsingou recurrence [13,14], dam-break dynamics [15,16], the kinetics of soliton gases and integrable turbulence [17,18], dispersive hydrodynamics driven by shock waves [19,20], and other solitonic structures [21–23].

The picture radically changes for multidimensional systems. Passing from $(1+1)$D to $(2+1)$D can cause irreversible loss of integrability, as happens for the cubic NLS. In this case, 1D solitons become unstable against transverse periodic perturbations in the additional dimension [24–26], while 2D solitons, which are no longer expressible in closed form, either undergo collapse in the focusing (attractive) case [27] or require a topological charge to be stabilized in the form of vortices in the defocusing (repulsive) case [28,29]. On the other hand, there are hydrodynamic models such as the two forms of the Kadomtsev-Petviashvili (KP) equation [30,31], known as KPI and KPII, which retain an integrable structure with closed-form soliton solutions. Unlike the KPII, which supports stable line (1D) solitons forming weblike structures [32–34], in the KPI model, line solitons are unstable [35,36], and the only stable analytical solution is the *lump soliton*. However, the KPI can hardly describe

*Contact author: ludovica.dieli@uniroma1.it
†Contact author: davide.pierangeli@uniroma1.it

accessible experiments, since it corresponds to a hydrodynamic regime where surface tension dominates over gravity, a condition that never holds for oceanic waves [37] and is extremely arduous to realize in fluids.

Lump solitons are rational analytic solutions localized in 2D and free of topological charge, which propagate unchanged and interact elastically with other lumps. Predicted in 1977 [38] for the KPI [39–43], they are still the object of theoretical efforts aimed at generalizing to higher-order solutions [44–47] and exist also in other multidimensional integrable models [48–50]. Despite such theoretical advances, lumps have never been observed [51]. This lack of experimental evidence challenges the effective universality of integrable models and their significance when passing from the realm of math to physical reality. For this reason, an observation of lump solitons would have a potential impact in fostering further applications of nonlinear waves and developing related theories.

To observe the lump of the KPI, we exploit that, in the hydrodynamic description of the defocusing $(2+1)$D NLS [19], the dynamics of a shallow 2D density depression standing over an intense flat background is described by the KPI [52–54]. The intrinsic anisotropy of the KPI is recovered in the isotropic $(2+1)$D NLS by the introduction of a nonsymmetric phase term, which is responsible for an unavoidable rigid translation of the lump in a given direction of the transverse plane. This connection between the KPI and the $(2+1)$D NLS guarantees that the observed lumps can form in other physical systems involving envelope wave packets in shallow water and in superfluids like BECs or exciton polaritons [52,55–58].

Here, we present the first experimental observation of the fundamental lump soliton of the KPI. We employ a paraxial light beam in a nonlinear optical medium. The regime ruled by the KPI is observed by propagating a laser beam along the z-axis of a bulk crystal with diffraction in the transverse (x,y) plane. An innovative waveform shaping platform allows precise generation of the input analytical shape of the lump soliton. By tuning the nonlinear response of the crystal, we explore the conditions for the integrable regime, which gives rise to undistorted propagation of the excited lump. We accurately determine how the translational velocity of the lump depends on its intensity dip, which is a distinctive feature of the KPI regime with respect to $(2+1)$D NLS solitons. Finally, the integrable behavior of the lump is proved by observing shape-preserving 2D collisions.

The lump soliton in $(2+1)$D *systems*—The KPI equation for a $(2+1)$D scalar field $\eta(X,Y,Z)$,

$$(-\eta_Z - 6\eta\eta_X + \eta_{XXX})_X - 3\eta_{YY} = 0, \tag{1}$$

admits a family of rational algebraic solutions known as lump solitons [51], defined via the ε parameter that fixes the lump amplitude and width:

$$\eta(X,Y,Z) = -4\frac{\varepsilon^{-1} - (X+3\varepsilon Z)^2 + \varepsilon Y^2}{[\varepsilon^{-1} + (X+3\varepsilon Z)^2 + \varepsilon Y^2]^2}. \tag{2}$$

The lump is a well of maximum depth $\eta(0,0,0) = -4\varepsilon$ on the (X,Y) plane. Its solitonic nature gives a shape unaffected by the propagation along Z [Fig. 1(a)]. The lack of invariance for inversion of the X-axis in Eq. (1) causes the lump to shift along X during the propagation. The X displacement linearly depends on ε, $\Delta X(Z) = -3\varepsilon Z$, defining the lump velocity as $c = -3\varepsilon$. Integrability guarantees the preservation of the lump shape even when a collision occurs. Figure 1(b) illustrates this key feature: the elastic collision that distinguishes the lump from any nonintegrable 2D soliton [59].

Multidimensional nonlinear systems, such as water waves, photon fluids, and BECs, are described by the $(2+1)$D NLS for the dimensionless envelope $\psi = \psi(x,y,z)$ [51]:

$$i\psi_z + (\psi_{xx} + \psi_{yy})/2 + \gamma|\psi|^2\psi = 0. \tag{3}$$

In the defocusing $(2+1)$D NLS ($\gamma < 0$), an integrable regime described by the KPI is possible. In the hydrodynamic limit, the equivalence between the NLS [Eq. (3)] and the KPI [Eq. (1)] is proven in a uniformly moving reference frame $(x - c_0 z, y, z)$ by writing the lump as a small perturbation of a uniform background with normalized intensity ρ_0 and relative phase $\gamma\rho_0 z$ through the ansatz $\psi = \sqrt{\rho_0 + \eta}\exp(i\gamma\rho_0 z + i\phi)$. Here, $c_0 = \sqrt{-\gamma\rho_0}$ is the so-called speed of sound, the natural velocity of small perturbations generated over the strong background ρ_0 [52]. The isotropic behavior in the (x,y) plane is broken by the introduction of the phase profile $\phi = \phi(x - c_0 z, y, z)$, nonsymmetric along x, that is imprinted in the complex envelope ψ to support the lump, as shown in Fig. 1(c).

Relying on the asymptotic reduction of the NLS to the KPI [52] [see Supplemental Material (SM) [60]], the dark lump of the NLS is characterized by the following profiles of the square amplitude deviation from the background and the nonlinear phase of the complex envelope,

$$\eta(x,y,z) = \frac{2}{\gamma}\frac{\varepsilon^{-1} - (x - c_0 z + c_0/2\varepsilon z)^2 + \varepsilon y^2}{[\varepsilon^{-1} + (x - c_0 z + c_0/2\varepsilon z)^2 + \varepsilon y^2]^2},$$
$$\phi(x,y,z) = -\frac{2}{c_0}\frac{x - c_0 z + \varepsilon c_0/2z}{\varepsilon^{-1} + (x - c_0 z + c_0/2\varepsilon z)^2 + \varepsilon y^2}, \tag{4}$$

where the amplitude η is equivalent to the KPI lump in Eq. (2) with $X = x - c_0 z$, $Y = y$, and $Z = z$, and the phase follows from the compatibility condition $\phi_X = -(\gamma/c_0)\eta$ [52]. The lump arises on a plateau ρ_0 [Fig. 1(c)] and shifts along x with velocity $c = c_0(1 - \varepsilon/2)$. The parameter ε must be small for the reduction to be valid. Figure 1(c) shows how ε becomes the smallness scale required to pass from the nonintegrable hydrodynamic to the KPI regime, with the negative sign of γ that guarantees the defocusing case for the lump realization. According to the perturbative expansion, the equivalence between Eqs. (1) and (3) is

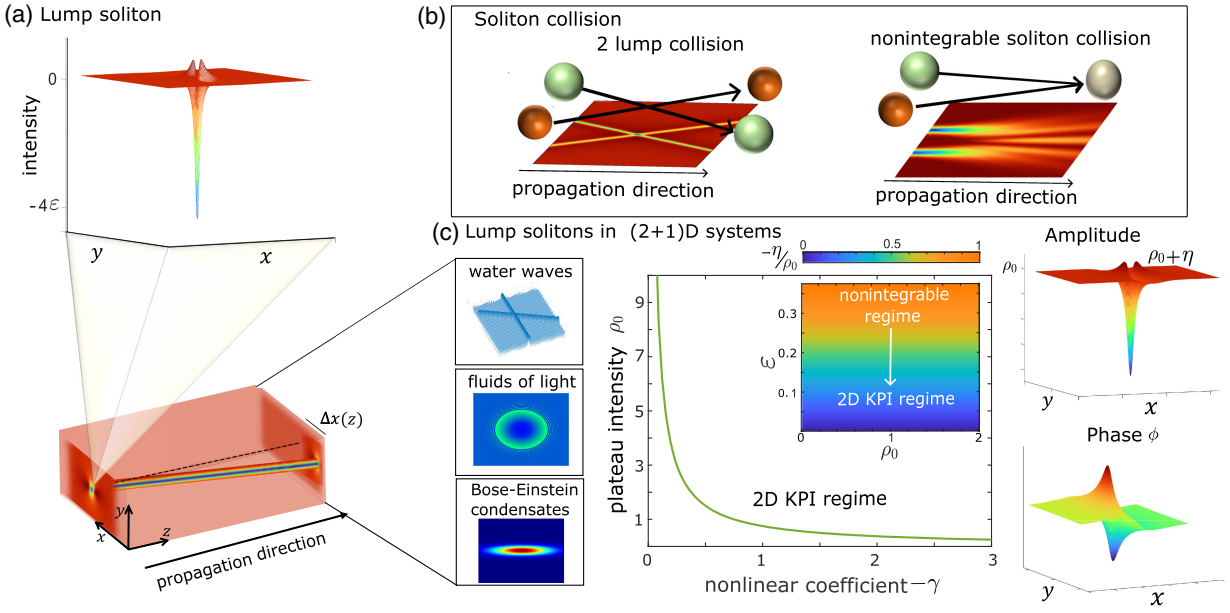

FIG. 1. Integrable solitons in $(2+1)$D systems. (a) The lump soliton is an ε-dependent family of analytical solutions of the KPI equation. The KPI anisotropy causes the lump to shift linearly along x during propagation. (b) Integrability determines the lump preservation in collisions, a fundamental difference with any nonintegrable 2D soliton. (c) In NLS systems, the KPI regime is found in the hydrodynamic limit by shaping the lump amplitude (η) and phase (ϕ) as a small perturbation over a flat background (ρ_0). The phase profile ϕ breaks the system isotropy. The integrable regime occurs when the plateau intensity ρ_0 is tuned according to the nonlinearity strength γ (green curve). The KPI description is more accurate the smaller ε [pseudocolor plot of $-\eta/\rho_0$ in the (ρ_0, ε) plane].

verified when the plateau intensity ρ_0 is tuned according to the dimensionless nonlinear coefficient γ to satisfy the relation $\rho_0 = 3/(4|\gamma|)$ [Fig. 1(c)]. A smaller plateau ρ_0 is required with larger $|\gamma|$, establishing the integrability condition that realizes the KPI regime in NLS systems. As a consequence, the speed of sound is fixed to $c_0 = \sqrt{-\gamma\rho_0} = \sqrt{3/4}$. In SM [60], the importance of the integrability condition is investigated by simulations and experiments. Moreover, ρ_0 bounds the depth of the lump: the constraint $\rho_0 + \min(\eta) > 0$ implies $0 < \varepsilon < 3/8$. In the limit $\varepsilon = 0$, the lump velocity c tends to c_0, but the soliton becomes infinitely shallow (vanishing depth). In our experiments, we trade off between the necessity to have a deep minimum in the dark lump and a velocity close to the speed of sound, choosing values in the range $\varepsilon = 0.1$–0.3. This results in velocity ratios $c/c_0 = 0.85$–0.95 that are sufficiently close to 1 for the KPI to be valid [53,61].

A crucial point lies in the nature of the x displacement. In the KPI, the shift is a property of the equation, whereas in the NLS, it is related to the initial condition. This allows us to control the lump shifting direction in the (x, y) plane by a simple rotation of both the lump phase and amplitude, producing a rotated lump. We can simultaneously generate different lumps oriented in different directions (see SM [60]). This feature is a powerful tool for exploring collisions between lumps and proving their integrable nature.

Observation of the lump soliton—The experiment relies on the nonlinear propagation of a laser beam in a photorefractive crystal [Fig. 2(a)]. A time-dependent nonlinear response is induced by an applied voltage V. The crystal refractive index n_0 is modified by the impinging intensity $I = |E|^2$ as $n(V,t) = n_0 + \delta n(V,t)I$. Given the crystal tetragonal symmetry, the sign of δn depends on the external field direction. We set the polarity to have a defocusing nonlinearity, the opposite of Ref. [26], where the setup is used to study 2D soliton gases. The optical field propagation in the physical space (lab frame) $(\bar{x}, \bar{y}, \bar{z})$ is described by Eq. (A1) in the End Matter, which is related to the theoretical model of Eq. (3) by a change of variables. The integrability condition translates in the experiment as a relation between the intensity I_0 and the experimental parameters V and t, defining the surface reported in Fig. 2(b), which gives the experimental parameters for which the lump can be observed.

The laser beam is prepared according to the NLS lump [Eq. (4)] and sent on the crystal input facet. The experimental setup is reported in Fig. 2(a) and detailed in the End Matter. The measurement is a time record of the beam intensity at the crystal output. Figure 2(c) reports the initial condition generated at the crystal input and the output at different time instants for fixed and constant V and I_0. As time passes, the parameters (V, t, I_0) move along the red arrow in Fig. 2(b) and, when they reach the surface of the integrability condition, the KPI regime is realized and the lump observed. Numerical simulations show the output intensity by varying γ, which corresponds to different parameters V, t.

In Fig. 3, we summarize the outcome of the experiments at two different values of $\varepsilon = 0.1$, 0.2 (velocity ratio $c/c_0 = 0.95$, 0.9) in comparison with numerical results.

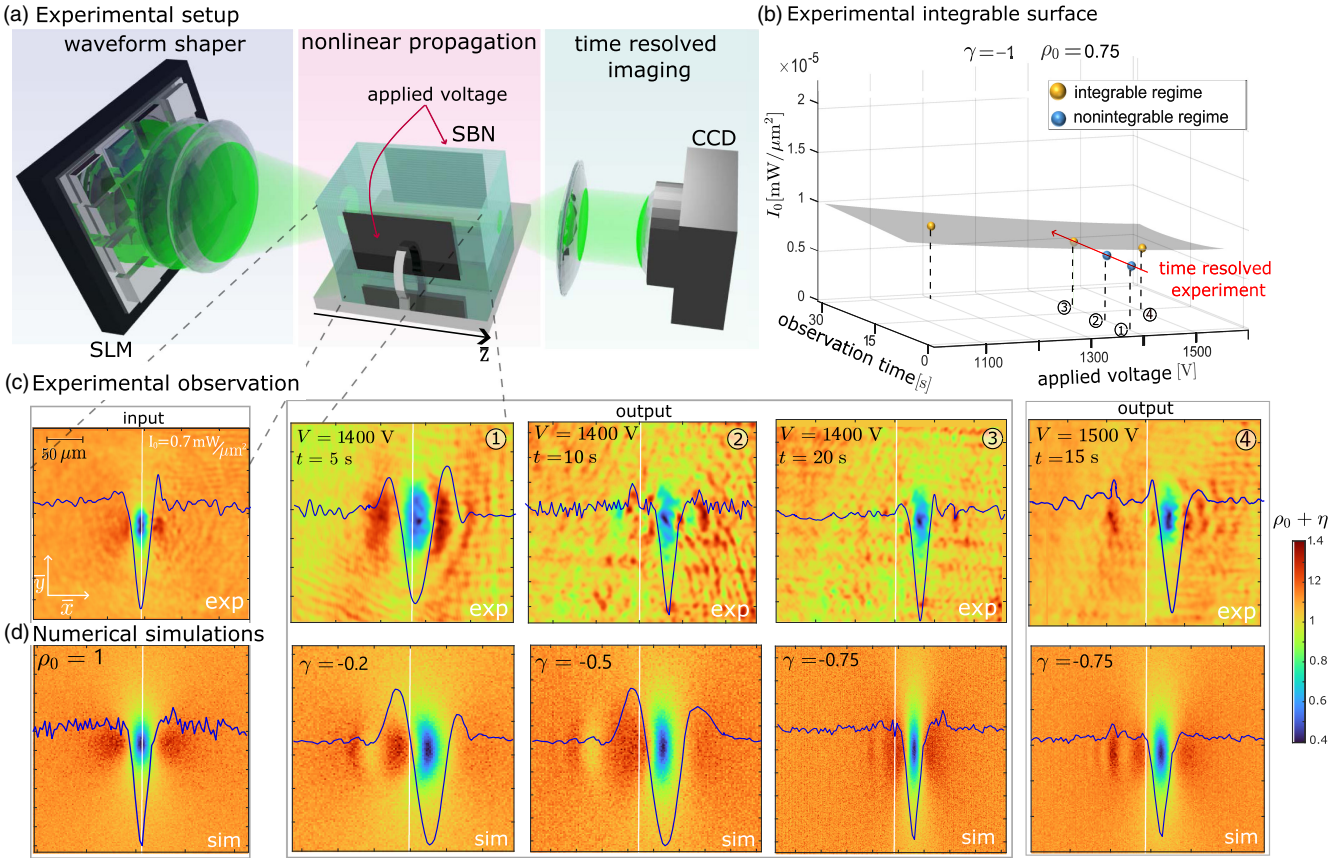

FIG. 2. Experimental realization of the lump soliton. (a) Sketch of the experimental setup. The initial condition is prepared by a waveform shaper based on a spatial light modulator (SLM). Nonlinear propagation occurs in a photorefractive SBN crystal. A camera (CCD) acquires the intensity at different time instants. (b) The experimental parameters, V, t, and I_0, must be precisely tuned to observe the KPI regime. The graph reports the surface on which they must be set to observe the lump. The golden points are sets of parameters for which the lump is observed, whereas the blue ones do not allow for the lump formation. (c) The input lump on an intensity plateau I_0 and as observed at the crystal output at different times for the four conditions in (b), showing how the integrability surface is approached as time varies at constant V. The intensity (dimensionless units) is normalized to I_0. (d) Numerical results showing the correspondence between the parameters (V, t) and γ with $\rho_0 = 1$.

Figure 3(a) shows the initial condition observed on the crystal input ($\bar{z} = 0$). The agreement between experimental and numerical data confirms the high accuracy of the beam shaping method. The lump with $\varepsilon = 0.1$ is wider and less deep than for $\varepsilon = 0.2$. Figure 3(b) reports its linear propagation. The field is observed at the output $\bar{z} =$ 5 mm when no voltage is applied. The lump waveform diffracts through the medium, losing its characteristic shape and producing higher and nonsymmetric peaks. The KPI regime is shown in Fig. 3(c). Nonlinear propagation is observed at $t = 20$ s with $V = 1400$ V. The lump shape is preserved during propagation and shifted toward the positive $\bar{x}$-axis. From the intensity $\bar{x}$ profile, we extract the experimental parameters of the lump (see SM [60]). The measured parameters (Table I) are in agreement with the theoretical and numerical values within experimental uncertainties. In SM [60], we report results for (V, t, I_0) that do not satisfy the integrability condition, which show how the integrable regime is not observed outside of the surface in Fig. 2(b). Experiments suggest the integrability condition is robust to the uncertainty of the parameters and noise. Thus, the integrability surface can be represented as a layer of finite thickness.

Lump velocity—The lump transverse displacement occurs with a ε-dependent velocity $c = c_0(1 - \varepsilon/2)$. We measure the lump speed from the observed displacement $\Delta\bar{x}$ evaluated as the difference between the position of the minimum of η at $\bar{z} = 0$ and $\bar{z} = 5$ mm. Figure 4 reports the measurement of the speed $c(\varepsilon) = \Delta\bar{x}(\varepsilon)/\bar{z}$ as a function of ε. Experimental data correspond to the sets of parameters of Fig. 2(b). The inset in Fig. 4 shows the expected displacement, with colors that encode the varying ε (we set $c_0 = \sqrt{3/4} = 0.87$; see SM [60]). This behavior reflects the subsonic nature of the soliton, as the fan of possible displacements is always below the speed of sound, c_0. The slopes of the linear displacements give the theoretical curve in Fig. 4. The relation $\Delta x = c_0(1 - \frac{1}{2}\varepsilon)z$ is verified using the extracted parameters, finding $c_0 = \sqrt{-\gamma\rho_0} = 0.92 \pm 0.09$, in agreement with the theoretical value.

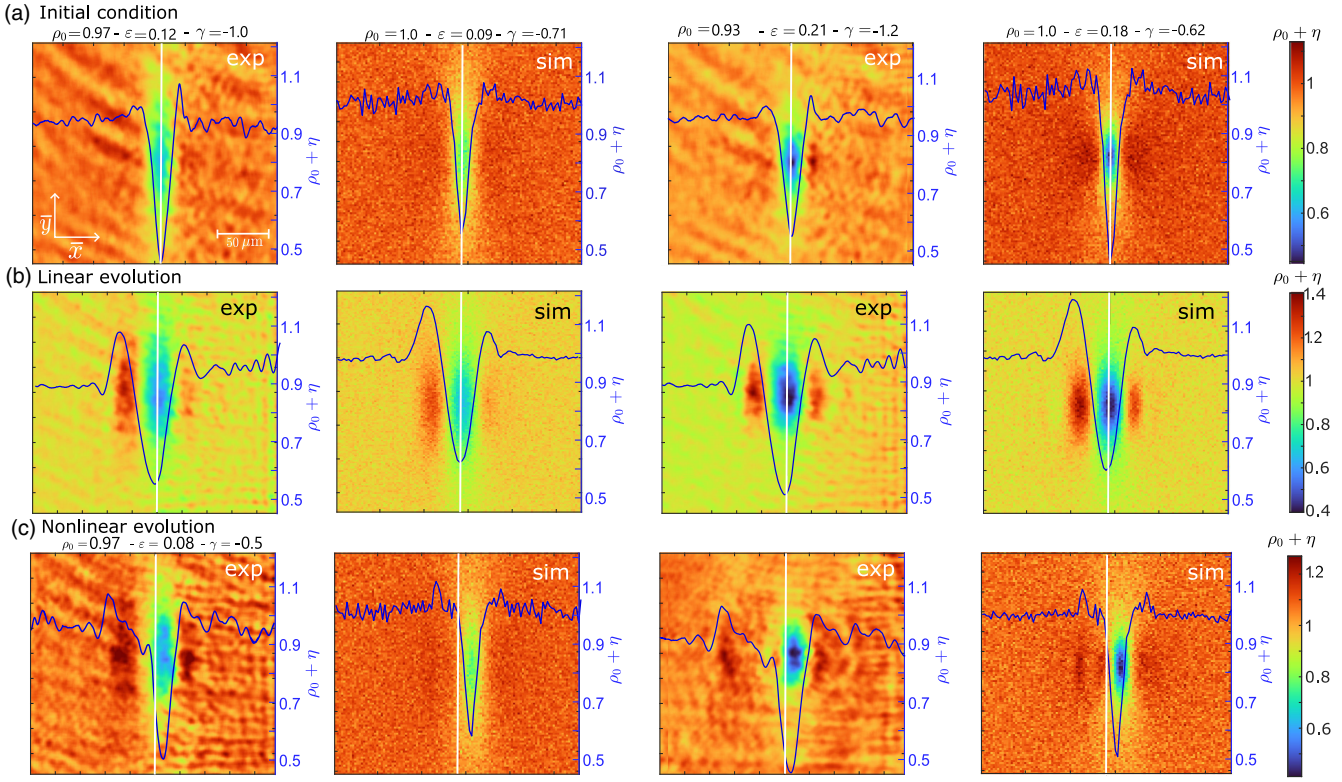

FIG. 3. Observation of lumps in a photon fluid. (a) Initial condition. Experimental data (exp) at $\bar{z} = 0$ and simulations (sim). The nominal parameters are $\rho_0 = 1, \gamma = -0.75$, and $\varepsilon = 0.1$ (left), $\varepsilon = 0.2$ (right). (b) Evolution at $\bar{z} = 5$ mm in linear condition ($V = 0$). (c) Nonlinear evolution for $V = 1400$ V and $t = 20$ s. Blue lines are profiles along $\bar{x}$ by averaging over $\bar{y}$. The effective parameters ρ_0, γ, and ε are derived from these profiles (Table I). The white vertical line marks the initial position of the lump to highlight the $\bar{x}$ displacement.

Elastic collision of two lumps—Collisions between lumps are expected to be elastic [38]. The ε-dependent speed suggests considering the interaction of lumps with different values of ε to see how the faster lump surpasses the slower one without affecting its nature [52]. The NLS lump x displacement is due to its phase shape. We exploit this fact to observe lumps displaced along different directions in the (x, y) plane. In SM [60], we report rotated lumps and their evolved states. Figure 5 reports the observation of a collision between two lumps characterized by the same ε but moving in different directions. We prepare two initial lumps with $\varepsilon = 0.2$ and choose their position on the (x, y) plane to observe them converging to the same point. The vertical lump is right shifting along x, while the other oblique-shifting lump is obtained by a rotation of $-5\pi/4$.

The interacting evolution of the lumps is observed at different $\bar{z}$ (Fig. 5). We achieve distances $\bar{z}$ longer than the physical length of the crystal by using the measured state at the output as a new input. The result in Fig. 5 raises key considerations. (i) Waveform shaping allows the generation of rotated lumps that retain their characteristics, guaranteeing full control of the displacement direction. (ii) The collision produces a state in which the lumps are no longer distinguishable. From this state, the lumps emerge as two distinct objects with their own shapes. (iii) After the

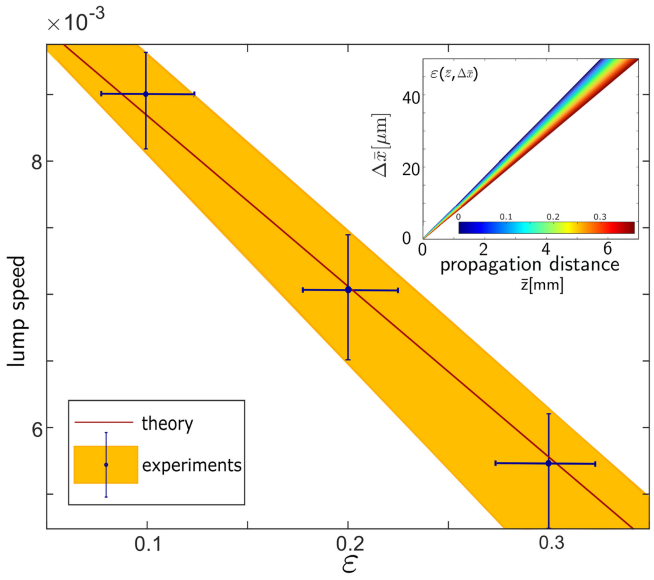

FIG. 4. The lump speed. Predicted speed (red curve) compared with experimental data (blue points) for $\varepsilon = 0.1, 0.2, 0.3$. The yellow shadow is the experimental error (standard deviation). The inset shows the theoretical prediction of $\Delta\bar{x}$ versus $\bar{z}$ for the allowed ε values.

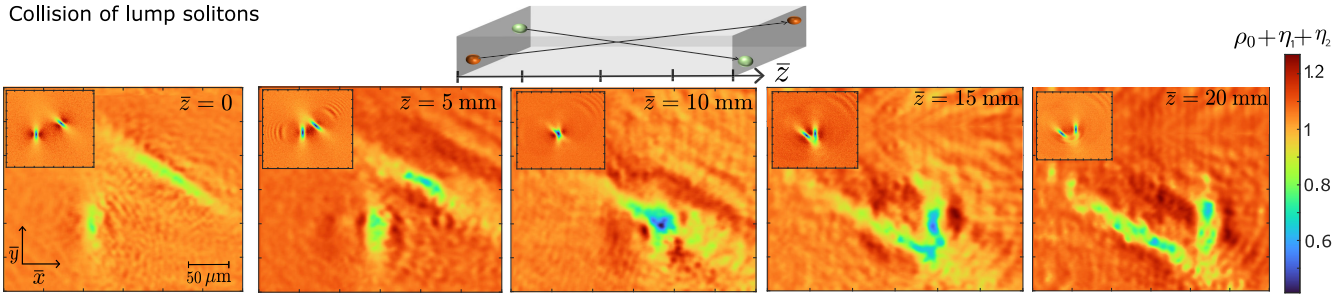

FIG. 5. Elastic collision of lumps. A right-shifting and an oblique-shifting lump are positioned in distant points at $\bar{z}=0$. The two lumps have $\epsilon=0.2$. During the $\bar{z}$ propagation, the lumps get closer due to their displacements. At $\bar{z}=10$ mm, the lumps experience a collision. They emerge from the collision keeping their localized shapes, as shown by their intensity at $\bar{z}=20$ mm. Insets show the corresponding simulated dynamics.

collision, the lumps continue their propagation in accordance with their initial conditions since the collision has not affected their shapes. This observation reveals the existence of analytical solitons in the $(2+1)$D NLS that behave in the collision as taking memory of their original integrable nature. On the contrary, $(2+1)$D NLS solitons not described by the KPI limit are expected to exchange energy and momentum in their interactions, leading to nonelastic collisions and potential vortex nucleation [62].

Conclusions—We have reported the first experimental evidence of lump solitons in one-to-one correspondence to the only stable one-parameter exact solutions of the integrable $(2+1)$D KPI equation. We have also demonstrated the observability of the elastic collision of multiple noncollinear lumps. Our experimental results rely on the knowledge of the analytical lump solution and on the accurate choice of the lump parameters so that the dynamics is described by the integrable KPI, which limits the soliton velocity to be close to the speed of sound. In our experiments, $c/c_0=0.85$–0.95. In this respect, our Letter addresses a regime that is fully distinct and complementary to recent results [63] aimed at exploring the so-called Jones-Roberts solitons [53] of the defocusing $(2+1)$D NLS in the regime where such solitons exhibit a smooth dynamic transition from a vortex dipole to a single rarefaction dip. In particular, Ref. [63] reports no evidence that the rarefaction dip quantitatively agrees with lumps of the KPI since the dip is observed in a range of smaller velocities ($c/c_0\sim 0.61$–0.8) and only as a transient phenomenon intentionally driven by a nonhomogeneous background [64].

In conclusion, our results show the experimental accessibility of high-dimensional integrable dynamics and establish our platform as an effective alternative to other photon or quantum fluid platforms to study many novel phenomena related to the KP, such as transverse instabilities or web structures of line solitons and multidirectional soliton gases [65,66]. Our observations bridge the gap between the many outstanding theoretical developments in the KP framework and the absence of direct experimental confirmations.

Acknowledgments—We acknowledge funding from HORIZON EIC-2022-PATHFINDERCHALLENGES-01 HEISINGBERG No. 101114978; the EU-NextGenerationEU under the National Recovery and Resilience Plan with PRIN Projects No. 2022597 MBS PHERMIAC, No. 2022N738SA MetaComputing, No. 20222NCTCY, and No. 2020X4T57A; the National Quantum Science and Technology Institute No. PE0000023-NQSTI; and the European Union HORIZON-ERC-2025-ADG HYPERSPIM No. 101139828, HORIZON-ERC-2024-STG LOOP No. 101162173.

Views and opinions expressed are those of the authors only and do not necessarily reflect those of the European Union or the European Research Council. Neither the European Union nor the granting authority can be held responsible for them.

Data availability—The data that support the findings of this article are not publicly available. The data are available from the authors upon reasonable request.

[1] S. Novikov, S. V. Manakov, L. P. Pitaevskii, and V. E. Zhakarov, *Theory of Solitons. The Inverse Scattering Method* (Plenum, New York, 1984).
[2] M. Ablowitz and H. Segur, *Solitons and the Inverse Scattering Transform* (SIAM, Philadelphia, 1981).
[3] J. H. V. Nguyen, P. Dyke, D. Luo, B. A. Malomed, and R. G. Hulet, Collisions of matter-wave solitons, Nat. Phys. **10**, 918 (2014).
[4] B. Kibler, J. Fatome, C. Finot, G. Millot, F. Dias, G. Genty, N. Akhmediev, and J. M. Dudley, The peregrine soliton in nonlinear fibre optics, Nat. Phys. **6**, 790 (2010).
[5] A. Romero-Ros, G. C. Katsimiga, S. I. Mistakidis, S. Mossman, G. Biondini, P. Schmelcher, P. Engels, and P. G. Kevrekidis, Experimental realization of the peregrine soliton in repulsive two-component Bose-Einstein condensates, Phys. Rev. Lett. **132**, 033402 (2024).
[6] A. Tikan, C. Billet, G. El, A. Tovbis, M. Bertola, T. Sylvestre, F. Gustave, S. Randoux, G. Genty, P. Suret,

and J. M. Dudley, Universality of the peregrine soliton in the focusing dynamics of the cubic nonlinear Schrödinger equation, Phys. Rev. Lett. **119**, 033901 (2017).
[7] B. Kibler, A. Chabchoub, A. Gelash, N. Akhmediev, and V. E. Zakharov, Superregular breathers in optics and hydrodynamics: Omnipresent modulation instability beyond simple periodicity, Phys. Rev. X **5**, 041026 (2015).
[8] D. R. Solli, C. Ropers, P. Koonath, and B. Jalali, Optical rogue waves, Nature (London) **450**, 1054 (2007).
[9] Y. V. Bludov, V. V. Konotop, and N. Akhmediev, Matter rogue waves, Phys. Rev. A **80**, 033610 (2009).
[10] M. Onorato, S. Residori, U. Bortolozzo, A. Montina, and F. Arecchi, Rogue waves and their generating mechanisms in different physical contexts, Phys. Rep. **528**, 47 (2013).
[11] S. Trillo, G. Deng, G. Biondini, M. Klein, G. F. Clauss, A. Chabchoub, and M. Onorato, Experimental observation and theoretical description of multisoliton fission in shallow water, Phys. Rev. Lett. **117**, 144102 (2016).
[12] C. Conti, A. Fratalocchi, M. Peccianti, G. Ruocco, and S. Trillo, Observation of a gradient catastrophe generating solitons, Phys. Rev. Lett. **102**, 083902 (2009).
[13] D. Pierangeli, M. Flammini, L. Zhang, G. Marcucci, A. J. Agranat, P. G. Grinevich, P. M. Santini, C. Conti, and E. DelRe, Observation of Fermi-Pasta-Ulam-Tsingou recurrence and its exact dynamics, Phys. Rev. X **8**, 041017 (2018).
[14] A. Mussot, C. Naveau, M. Conforti, A. Kudlinski, F. Copie, P. Szriftgiser, and S. Trillo, Fibre multi-wave mixing combs reveal the broken symmetry of Fermi–Pasta–Ulam recurrence, Nat. Photonics **12**, 303 (2018).
[15] G. Xu, M. Conforti, A. Kudlinski, A. Mussot, and S. Trillo, Dispersive dam-break flow of a photon fluid, Phys. Rev. Lett. **118**, 254101 (2017).
[16] G. Marcucci, D. Pierangeli, A. J. Agranat, R.-K. Lee, E. DelRe, and C. Conti, Topological control of extreme waves, Nat. Commun. **10**, 5090 (2019).
[17] I. Redor, E. Barthélemy, H. Michallet, M. Onorato, and N. Mordant, Experimental evidence of a hydrodynamic soliton gas, Phys. Rev. Lett. **122**, 214502 (2019).
[18] A. Gelash, D. Agafontsev, V. Zakharov, G. El, S. Randoux, and P. Suret, Bound state soliton gas dynamics underlying the spontaneous modulational instability, Phys. Rev. Lett. **123**, 234102 (2019).
[19] W. Wan, S. Jia, and J. W. Fleischer, Dispersive superfluid-like shock waves in nonlinear optics, Nat. Phys. **3**, 46 (2007).
[20] G. El and M. Hoefer, Dispersive shock waves and modulation theory, Physica (Amsterdam) **333D**, 11 (2016).
[21] G. G. Rozenman, L. Shemer, and A. Arie, Observation of accelerating solitary wavepackets, Phys. Rev. E **101**, 050201(R) (2020).
[22] M. Onorato, L. Cavaleri, S. Randoux, P. Suret, M. I. Ruiz, M. De Alfonso, and A. Benetazzo, Observation of a giant nonlinear wave-packet on the surface of the ocean, Sci. Rep. **11**, 23606 (2021).
[23] P. Jiang, N. Li, and J. Chen, Observation of kinked soliton structure in realistic materials through wave packet simulations, Phys. Lett. A **451**, 128409 (2022).
[24] E. Kuznetsov and S. Turitsyn, Instability and collapse of solitons in media with a defocusing nonlinearity, Zh. Eksp. Teor. Fiz. **94**, 129 (1988).
[25] D. E. Pelinovsky, Y. A. Stepanyants, and Y. S. Kivshar, Self-focusing of plane dark solitons in nonlinear defocusing media, Phys. Rev. E **51**, 5016 (1995).
[26] L. Dieli, D. Pierangeli, E. DelRe, and C. Conti, Observation of two-dimensional dam break flow and a gaseous phase of solitons in a photon fluid, Phys. Rev. Lett. **133**, 183801 (2024).
[27] K. D. Moll, A. L. Gaeta, and G. Fibich, Self-similar optical wave collapse: Observation of the townes profile, Phys. Rev. Lett. **90**, 203902 (2003).
[28] G. A. Swartzlander Jr and C. T. Law, Optical vortex solitons observed in Kerr nonlinear media, Phys. Rev. Lett. **69**, 2503 (1992).
[29] S. Donadello, S. Serafini, M. Tylutki, L. P. Pitaevskii, F. Dalfovo, G. Lamporesi, and G. Ferrari, Observation of solitonic vortices in Bose-Einstein condensates, Phys. Rev. Lett. **113**, 065302 (2014).
[30] B. B. Kadomtsev and V. I. Petviashvili, On the stability of solitary waves in weakly dispersing media, Doklady Akademii Nauk UzSSR **192**, 753 (1970).
[31] M. J. Ablowitz and H. Segur, On the evolution of packets of water waves, J. Fluid Mech. **92**, 691 (1979).
[32] Y. Kodama, *KP Solitons and the Grassmannians. Combinatorics and Geometry of Two-Dimensional Wave Patterns* (Springer, Singapore, 2017), Vol. 97.
[33] G. Biondini and S. Chakravarty, Soliton solutions of the Kadomtsev-Petviashvili II equation, J. Math. Phys. (N.Y.) **47**, 033514 (2006).
[34] G. Biondini, Line soliton interactions of the Kadomtsev-Petviashvili equation, Phys. Rev. Lett. **99**, 064103 (2007).
[35] D. Pelinovsky and Y. A. Stepanyants, Self-focusing instability of plane solitons and chains of two-dimensional solitons in positive-dispersion media, Sov. Phys. JETP **77**, 602 (1993).
[36] E. Infeld, A. Senatorski, and A. A. Skorupski, Decay of Kadomtsev-Petviashvili solitons, Phys. Rev. Lett. **72**, 1345 (1994).
[37] A. R. Osborne, *Nonlinear Ocean Waves and the Inverse Scattering Transform* (Academic Press, London, 2010), Vol. 97.
[38] S. Manakov, V. Zakharov, L. Bordag, A. Its, and V. Matveev, Two-dimensional solitons of the Kadomtsev-Petviashvili equation and their interaction, Phys. Lett. **63A**, 205 (1977).
[39] R. Johnson and S. Thompson, A solution of the inverse scattering problem for the Kadomtsev-Petviashvili equation by the method of separation of variables, Phys. Lett. **66A**, 279 (1978).
[40] J. Satsuma and M. J. Ablowitz, Two-dimensional lumps in nonlinear dispersive systems, J. Math. Phys. (N.Y.) **20**, 1496 (1979).
[41] D. Pelinovsky, Rational solutions of the Kadomtsev-Petviashvili hierarchy and the dynamics of their poles. I. New form of a general rational solution, J. Math. Phys. (N.Y.) **35**, 5820 (1994).
[42] A. Minzoni and N. Smyth, Evolution of lump solutions for the KP equation, Wave Motion **24**, 291 (1996).
[43] J. Villarroel and M. J. Ablowitz, On the discrete spectrum of the nonstationary Schrödinger equation and multipole lumps of the Kadomtsev-Petviashvili I equation, Commun. Math. Phys. **207**, 1 (1999).

[44] W.-X. Ma, Lump solutions to the Kadomtsev-Petviashvili equation, Phys. Lett. A **379**, 1975 (2015).
[45] P. Gaillard, Rational solutions to the KPI equation and multi rogue waves, Ann. Phys. (Amsterdam) **367**, 1 (2016).
[46] W. Hu, Z. Zhang, Q. Guo, and Y. Stepanyants, Solitons and lumps in the cylindrical Kadomtsev-Petviashvili equation. I. Axisymmetric solitons and their stability, Chaos **34**, 013138 (2024).
[47] Z. Zhang, W. Hu, Q. Guo, and Y. Stepanyants, Solitons and lumps in the cylindrical Kadomtsev-Petviashvili equation. II. Lumps and their interactions, Chaos **34**, 013132 (2024).
[48] D. J. Kaup, The lump solutions and the bäcklund transformation for the three-dimensional three-wave resonant interaction, J. Math. Phys. (N.Y.) **22**, 1176 (1981).
[49] C. Gilson and J. Nimmo, Lump solutions of the BKP equation, Phys. Lett. A **147**, 472 (1990).
[50] S. Chakravarty, S. Kent, and E. Newman, Some reductions of the self-dual Yang–Mills equations to integrable systems in $2+1$ dimensions, J. Math. Phys. (N.Y.) **36**, 763 (1995).
[51] M. J. Ablowitz, *Nonlinear Dispersive Waves: Asymptotic Analysis and Solitons* (Cambridge University Press, Cambridge, England, 2011), Vol. 47.
[52] F. Baronio, S. Wabnitz, and Y. Kodama, Optical Kerr spatiotemporal dark-lump dynamics of hydrodynamic origin, Phys. Rev. Lett. **116**, 173901 (2016).
[53] C. Jones and P. H. Roberts, Motions in a Bose condensate. IV. Axisymmetric solitary waves, J. Phys. A **15**, 2599 (1982).
[54] S. Tsuchiya, F. Dalfovo, and L. Pitaevskii, Solitons in two-dimensional Bose-Einstein condensates, Phys. Rev. A **77**, 045601 (2008).
[55] G. Huang, V. A. Makarov, and M. G. Velarde, Two-dimensional solitons in Bose-Einstein condensates with a disk-shaped trap, Phys. Rev. A **67**, 023604 (2003).
[56] T. P. Horikis and D. J. Frantzeskakis, Light meets water in nonlocal media: Surface tension analogue in optics, Phys. Rev. Lett. **118**, 243903 (2017).
[57] D. J. Frantzeskakis, T. P. Horikis, A. S. Rodrigues, P. G. Kevrekidis, R. Carretero-González, and J. Cuevas-Maraver, Hydrodynamics and two-dimensional dark lump solitons for polariton superfluids, Phys. Rev. E **98**, 022205 (2018).
[58] A. Villois, M. Onorato, and D. Proment, Vortex to rotons transition in dipolar Bose-Einstein condensates, Phys. Rev. Lett. **134**, 253401 (2025).
[59] F. Xin, F. Di Mei, L. Falsi, D. Pierangeli, C. Conti, A. J. Agranat, and E. DelRe, Evidence of chaotic dynamics in three-soliton collisions, Phys. Rev. Lett. **127**, 133901 (2021).
[60] See Supplemental Material at http://link.aps.org/supplemental/10.1103/ggbs-y21w for further details on the integrable regime of the NLS and lump solutions and additional measurements on rotated lumps.
[61] D. Chiron and M. Maris, Rarefaction pulses for the nonlinear Schrödinger equation in the transonic limit, Commun. Math. Phys. **326**, 329 (2014).
[62] N. G. Berloff, Padé approximations of solitary wave solutions of the Gross–Pitaevskii equation, J. Phys. A **37**, 1617 (2004).
[63] M. Baker-Rasooli, T. Aladjidi, N. A. Krause, A. S. Bradley, and Q. Glorieux, Observation of Jones-Roberts solitons in a paraxial quantum fluid of light, Phys. Rev. Lett. **134**, 233401 (2025).
[64] L. A. Smirnov and V. A. Mironov, Dynamics of two-dimensional dark quasisolitons in a smoothly inhomogeneous Bose-Einstein condensate, Phys. Rev. A **85**, 053620 (2012).
[65] T. Grava, C. Klein, and G. Pitton, Numerical study of the Kadomtsev–Petviashvili equation and dispersive shock waves, Proc. R. Soc. A **474**, 20170458 (2018).
[66] T. Bonnemain, G. Biondini, B. Doyon, G. Roberti, and G. A. El, Two-dimensional stationary soliton gas, Phys. Rev. Res. **7**, 013143 (2025).
[67] L. Falsi, A. Villois, F. Coppini, A. J. Agranat, E. DelRe, and S. Trillo, Evidence of $1+1$D photorefractive stripe solitons deep in the Kerr limit, Phys. Rev. Lett. **133**, 183804 (2024).
[68] O. Mendoza-Yero, G. Mínguez-Vega, and J. Lancis, Encoding complex fields by using a phase-only optical element, Opt. Lett. **39**, 1740 (2014).
[69] M. Mariş, Nonexistence of supersonic traveling waves for nonlinear Schrödinger equations with nonzero conditions at infinity, SIAM J. Math. Anal. **40**, 1076 (2008).
[70] T. W. Neely, E. C. Samson, A. S. Bradley, M. J. Davis, and B. P. Anderson, Observation of vortex dipoles in an oblate Bose-Einstein condensate, Phys. Rev. Lett. **104**, 160401 (2010).
[71] N. Meyer, H. Proud, M. Perea-Ortiz, C. O'Neale, M. Baumert, M. Holynski, J. Kronjäger, G. Barontini, and K. Bongs, Observation of two-dimensional localized Jones-Roberts solitons in Bose-Einstein condensates, Phys. Rev. Lett. **119**, 150403 (2017).

End Matter

Photorefractive lump—In the experiment, the optical field E propagates in a photorefractive crystal, where a time-dependent nonlinear response is induced by an externally applied voltage. The crystal refractive index becomes $n(V,t) = n_0 + \delta n(V,t)I$, with the impinging intensity $I = |E|^2$. The refractive index variation depends on the applied voltage V and on time t through the crystal response function $f(t)$, which accounts for charge motion in the bulk. The crystal response function $f(t) = (1 - e^{-t/\tau_s})$ also describes the saturation of the nonlinear effect due to charge recombination on a time scale τ_s, called saturation time. The nonlinear coefficient that rules the refractive index variation, in the nonsaturable limit valid low-intensity beams with respect to the background illumination [67], is written as $\delta n(V,t) = -(n_0^3 r_{33}/2L_x I_s)Vf(t)$, where r_{33} is the only relevant term of the electro-optic tensor of the crystal, I_s is the characteristic saturation intensity, and $L_{\bar{x}} = 5$ mm is the crystal size along $\bar{x}$. The model equation is

$$i\frac{\partial E}{\partial \bar{z}}+\frac{1}{2k}\left(\frac{\partial^2 E}{\partial \bar{x}^2}+\frac{\partial^2 E}{\partial \bar{y}^2}\right)+k\frac{\delta n}{n_0}|E|^2E=0, \quad \text{(A1)}$$

where $k=2\pi n_0/\lambda$ is the wave number.

The system description can be reduced to the dimensionless $(2+1)$D NLS [Eq. (3)] by the introduction of the physical parameters x_0 and I_0. We normalize the field $E=\sqrt{I_0}\psi$ and the spatial coordinates $\bar{x}=x_0x$, $\bar{y}=x_0y$, $\bar{z}=kx_0^2z$, and obtain the dimensionless nonlinear coefficient $\gamma=k^2[\delta n(V,t)/n_0]I_0x_0^2$. For the experimental realization, we can choose without loss of generality, $\gamma=-1$, finding $I_0(V,t)=-\frac{1}{k^2x_0^2}\frac{n_0}{\delta n(V,t)}$, where $x_0=8$ μm is chosen to fix the physical size of the lump. As a consequence, the regime ruled by the KPI is observed by tuning the beam intensity I_0 to the nonlinear response of the crystal, defined by V and t. From the choice $\gamma=-1$, the value of $\rho_0=3/4$ is fixed. As a consequence, the experimental lump has the characteristic form

$$E(\bar{x},\bar{y},\bar{z})=\sqrt{I_0\left(\frac{3}{4}+\eta\right)}\exp\left(i\gamma\rho_0\frac{\bar{z}}{kx_0^2}+i\phi\right), \quad \text{(A2)}$$

where η and ϕ are the NLS lump amplitude and phase reported in Eq. (4). The integrability condition $\rho_0=\rho_0(\gamma)$ is transposed in the experiment as $I_0=I_0(V,t)$, as reported in Fig. 2(b).

Experimental setup—The experimental setup is reported in Fig. 2(a). A waveform shaping platform is implemented to control the beam shape and prepare the initial condition. We use the holographic method developed in [68], which is based on the encoding of a complex field in a phase-only spatial light modulator (SLM, Hamamatsu X13138). The field phase and amplitude are encoded in the phases of two fields with constant amplitude, which are defined on two interpenetrating chessboards on the SLM. The shaping resolution is given by the chessboard period, in our experiment 25 μm. After the SLM, an objective reduces the shaped beam size by a factor of 0.125. The laser beam is prepared according to the lump soliton initial condition and sent on the input facet of the crystal. The nonlinear propagation of the beam (20 mW power) occurs in a photorefractive crystal of strontium barium niobate [SBN, $Sr_xBa_{(1-x)}Nb_2O_6$, with $x=0.61$] of size $5\times5\times5$ mm^3. The output facet of the crystal is imaged through a lens on a CCD camera, where the time evolution of the intensity of the propagating field is observed. The spatial resolution of detected intensity images is 0.35 μm. For each measurement, we take the image of the initial condition on the input facet of the crystal, the linear output, and the time evolution of the output after switching the voltage on.

Experimental and data analysis methods—We prepare the initial condition by fixing a specific value of the parameter ε. The experimental parameters V, t, and I_0 are chosen to fulfill the integrability condition of Fig. 2(b). Figure 2(b) shows the difference between sets of parameters that are not on the integrability surface (points 1 and 2) and the ones taken on the surface (points 3 and 4). For points 1 and 2, we do not observe the lump, but the propagated field has a deformed intensity shape. Points 3 and 4 are on the surface, and the lump is observed. Numerical simulations are reported to show that different sets of the experimental parameters I_0, V, and t correspond to different values of the nonlinear coefficient γ, and on the surface in Fig. 2(b), the integrability condition $\rho_0=3/(4|\gamma|)$ is satisfied.

TABLE I. Parameters extrapolated from the measured (exp) or simulated profiles (sim) in Fig. 3.

Parameters	Nominal $\varepsilon=0.1$		Nominal $\varepsilon=0.2$	
	Exp	Sim	Exp	Sim
$\varepsilon(0)$	0.12 ± 0.02	0.09 ± 0.01	0.21 ± 0.01	0.18 ± 0.02
$\rho_0(0)$	0.97 ± 0.05	1.0 ± 0.2	0.93 ± 0.05	1.0 ± 0.2
$\gamma(0)$	-1.0 ± 0.2	-0.71 ± 0.05	-1.2 ± 0.4	-0.62 ± 0.09
$\varepsilon(5$ mm$)$	0.08 ± 0.01	0.09 ± 0.01	0.19 ± 0.01	0.18 ± 0.02
$\rho_0(5$ mm$)$	0.97 ± 0.04	1.0 ± 0.2	0.95 ± 0.05	1.0 ± 0.2
$\gamma(5$ mm$)$	-0.5 ± 0.2	-0.71 ± 0.05	-0.9 ± 0.4	-0.62 ± 0.09

Experimental results are reported in dimensionless units. The intensity $\rho_0+\eta$ is obtained from the measured intensity by dividing by the background intensity of the initial condition I_0. To compare experimental data to the exact solution relative to the chosen value of ε, we fit the nonlinear wave profile. From this comparison, we extract the parameters reported in Table I.

Specifically, the lump parameters in Table I at $\bar{z}=0$ and $\bar{z}=5$ mm are extrapolated from the input (first row in Fig. 3) and output (third row in Fig. 3), respectively. Uncertainties are obtained by averaging over data samples obtained with the same parameters. All the parameters are dimensionless. The displacement $\Delta\bar{z}$ is measured by evaluating the position of the intensity minimum at different times. The minimum of η is taken as the weighted average over $\bar{x}$, in the region where $\eta<0$.

In Fig. 4, the experimental points at a fixed ε are obtained by averaging over data relative to different sets of parameters chosen on the surface in Fig. 2.

Validity of the KPI regime—In our experiment, we operate with translation velocities sufficiently close to the speed of sound, which is the only regime where the reduction to the KPI turns out to be accurate [53,61]. In general, solitons of the defocusing NLS are known to be subsonic [69], but as their velocity decreases, the description in terms of KPI loses validity until eventually, below a critical velocity, the soliton takes the form of a stable vortex dipole [53], as observed in experiments [63,70,71].

Numerical simulations—The dimensionless 2D NLS [Eq. (3)] is numerically solved through the beam propagation method using the lump initial condition [Eq. (4) at $z = 0$], γ as a free parameter, and $\rho_0 = 3/(4|\gamma|)$. In [60], we report simulations where the parameters do not satisfy the integrability condition. White noise is added to the initial condition to reproduce the nonperfect experimental conditions and to induce a nondeterministic dynamics.